J. Eur. Opt. Society-Rapid Publ. 2026, **22**, 9
© The Author(s), published by EDP Sciences, 2026
https://doi.org/10.1051/jeos/2026002
Available online at: https://jeos.edpsciences.org

Journal of the European Optical Society-Rapid Publications

Research Article — Open Access

Polarization camera based fringe locking system for scanning beam interference lithography

Kevin Treptow[1,*], Josias Rühle[2], Hansen Wu[1], Christof Pruß[1], Ingo Ortlepp[3], Christian Schober[1], Tobias Haist[1], Oliver Sawodny[2], Eberhard Manske[3], Thomas Kissinger[3], and Stephan Reichelt[1]

[1] Institute of Applied Optics (ITO), University of Stuttgart, Pfaffenwaldring 9, 70569 Stuttgart, Germany
[2] Institute for System Dynamics, University of Stuttgart, Waldburgstraße 19, 70563 Stuttgart, Germany
[3] Institute of Process Measurement and Sensor Technology, Technische Universität Ilmenau, Gustav-Kirchhoff-Str. 5, 98693 Ilmenau, Germany

Received 31 October 2025 / Accepted 9 January 2026

Abstract. A fringe displacement during the exposure process in scanning beam interference lithography (SBIL) systems leads to wavefront errors in linear gratings. The exact orientation of the fringe pattern along the scan direction is also essential for the production of high-quality gratings. In this paper, we report on the development of a fringe stabilization system with a separate measuring beam, which can precisely determine the fringe movement during the exposure of the photoresist and simultaneously record the orientation of the fringe pattern. This is specifically designed to minimize low-frequency phase errors originating in the lithography writing head itself, which can be a dominant source of instability independent of the stage positioning. Using polarization camera based phase-shifting interferometry, we determine the phase offset between the two interfering beams in real time, and thus reduce the fringe movement to single-digit nanometers by moving a piezo-actuated mirror. In addition, we can use the area-based phase measurement to align the setup and track the rotation of the fringe spot during exposure. In combination with a nano positioning and measuring machine, a fringe observation system was implemented that can precisely record the fringe displacement in the substrate plane. This allows the performance of the fringe stabilization system to be quantified.

Keywords: Laser lithography, Gratings, Diffractive elements.

1 Introduction

Diffractive gratings are used in various areas of optics. They are often integrated in optical metrology setups such as spectrometers [1] and interferometers [2], used in beam sources like monochromators, optical pulse compressing devices [3] and are used to shape the polarization [4]. The requirements for the precise fabrication of the gratings are constantly increasing. There are various approaches to producing these diffractive elements, depending on the size of the elements and the geometry of the substrate. A highly precise manufacturing technique for large substrate areas is mask lithography, especially EUV lithopgraphy [5]. However, the lithography mask is expensive and the setup is not flexible in manufacturing different elements. Direct laser writing [6, 7] offers a flexible process, but the structure size is limited by the spot width and the exposure times are long. Interference lithography [8] offers high-precision manufacturing for sub-wavelength structures on different substrate geometries and flexible grating periods. Due to the curved profile of the exposure beams, periodic chirping errors occur, which increases the wavefront error of the diffractive element [9]. Accordingly, the next approach is the scanning beam interference lithography. A small exposure spot is used to scan along the surface of the substrate. After every line, the position is shifted perpendicular to the scan direction and the next area will be scanned. Scanning beam interference lithography (SBIL) was first introduced by the Massachusetts Institute of Technology (MIT) in context of the "Nanoruler" [10]. The problem of phase errors between the two interference beams is well known. The environment disturbances such as vibrations, pressure changes, air turbulence and refractive index fluctuations are critical factors while fabricating linear gratings with sub-micron structures. There are different approaches for optical metrology systems and mechanical compensations to minimize these errors. In general, the two writing beams are directed by beam splitters and subsequently interfere on CCDs, PSDs and standard photodetectors [11–13]. Using the phase-shifting method of interferometry, the phase

* Corresponding author: kevin.treptow@ito.uni-stuttgart.de

This is an Open Access article distributed under the terms of the Creative Commons Attribution License (https://creativecommons.org/licenses/by/4.0), which permits unrestricted use, distribution, and reproduction in any medium, provided the original work is properly cited.

can be determined precisely. To enable real-time phase calculation, photo detectors are often used in combination with polarization optics [14]. However, phase errors are not the only challenge in SBIL systems. Precise adjustment and alignment of the optical components are also essential. Reference gratings and dedicated setups are commonly used for pre-alignment [15–18].

Polarization cameras have a pixelated polarizer array in front of the sensor. This offers area-based real-time interferometry. We will use this approach to implement a suitable fringe locking system to a SBIL writing head. Compared to commonly used photo diodes, the area-based fringe locking system provides not only the phase offset error between the interference beams, but also the rotational movements respectively the rotation of the wavefronts. In contrast to the Fourier-transform method [19], carrier frequencies are not needed to evaluate wavefronts. This provides a dynamic scope for this approach. In this paper, we present a compact design for an SBIL writing head, which is integrated into the nano-positioning and measuring machine NPMM-200 [20]. We evaluate the experimental performance of the fringe locking system using the polarization phase-shifting interferometry and demonstrate in situ angular tracking of the fringe pattern. In addition, for all performance tests, we verify the measurements with an independent fringe observation system.

2 Effects of fringe perturbation

The quality and accuracy of a diffractive grating crucially depends on the stability and orientation of the interference fringes. Disturbances lead to incorrectly exposed areas in the photoresist and thus directly influence the wavefront quality of the diffractive grating. An SBIL system consists of two main components: the writing head, which generates a small stationary interference pattern, and the stage positioning system, which scans the substrate beneath this pattern to produce extended linear gratings stripe by stripe. In this work, we present a solution that ensures the interference pattern remains stationary even in the presence of drift effects. This system will be integrated in the future into the overall control architecture illustrated in Figure 1, where it will also enable deliberate adjustments of the interference pattern to compensate for stage positioning errors. In contrast to the temporally high-frequency corrections that will be corrected in an 8333 Hz control-loop, the drift compensations of the writing head do require only control-loop frequency of a few ten Hertz due to the relatively slow drift variations.

Typical disturbances in the writing head are phase shifts, fringe pattern rotations and fringe period drifts. The different disturbances are simulated in Figure 2.

2.1 Phase shift

A phase shift occurs when the optical path lengths of the interfering beams change slightly, for instance due to thermal fluctuations or mechanical vibrations. This results in a shift of the fringes in the interference pattern perpendicular to the scanning direction. The period and the fringe

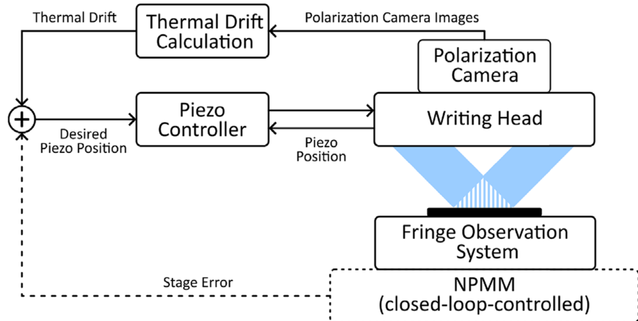

Figure 1. Control architecture of the SBIL writing head setup. The control systems of the lithography writing head and the positioning system NPMM-200 are separated. The dashed components are the scanning system into which the writing head will be included to form an SBIL system. For the performance evaluation presented in this work, a fringe observation system is mounted beneath the writing head on the NPMM-200 stage to monitor the resulting interference pattern.

orientation remain unchanged. Mechanical vibrations are high-frequency errors, but can be minimized by suitable damping of the system. Thermal fluctuations in the environment are low-frequency disturbances that are difficult to control. Therefore, the optical path lengths of the exposure beams are adjusted to compensate for fluctuations. In this paper, the phase shift is measured in an SBIL system and will be compensated by piezo-actuated mirror.

2.2 Period drift

The period drift is a change in the spatial period of the interference pattern. It is caused by drifts in the angle of incidence of the writing beams and also induces a phase shift. The change in the angle of incidence is usually caused by thermal movement of a mirror. Measurements on our system have shown that the mechanical and thermal stability of the writing head setup keeps period drifts (less than 150 ppm/h) in a region where it does not need to be considered.

2.3 Fringe pattern rotation

The rotation of the pattern is caused by a slight change in the angle between the interfering beams, which can be caused by insufficient pre-alignment or thermal expansion of the optical components. The result is a fringe pattern that rotates with respect to the intended scanning direction, which leads to poor dose contrast during exposure. While this is not a problem for our experimental system due to the low thermal drift (see Sect. 2.2), it still might be interesting to be controlled to follow yaw errors of the scanning stage.

2.4 Photoresist exposure and dose contrast loss

Perturbations in the interference pattern affect the photoresist exposure process itself. A stable and well-defined interference field is essential to produce a high-contrast intensity modulation in the resist. When phase shifts, period drifts

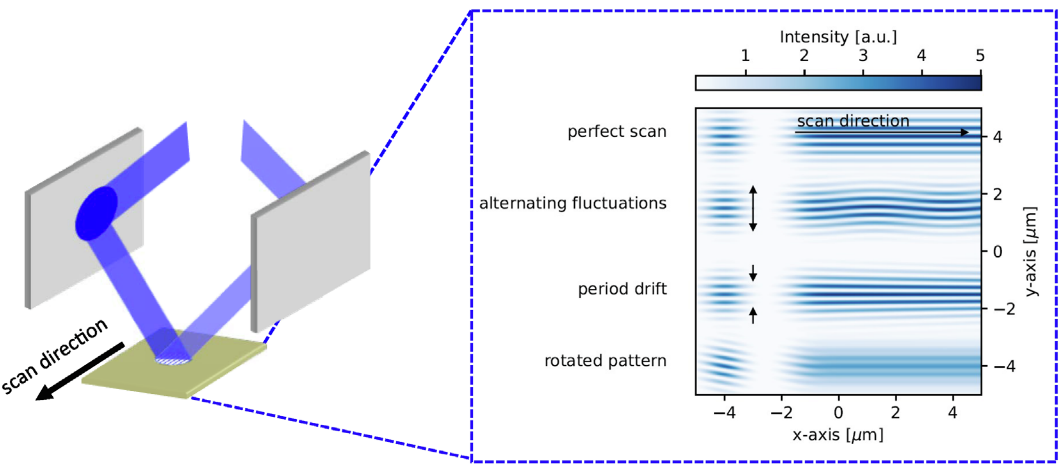

Figure 2. Left: Principle sketch of SBIL setup with two mirrors. Right: Simulation of SBIL in x-direction with different disturbances. The first scenario shows a perfect scan without disturbances. The second scenario shows the case in which the fringes in the exposure pattern move up and down alternately due to phase fluctuations and generate curved paths. In the next scenario, the angle of incidence drifts during scanning. This changes the period of the fringe during the exposure. In the last scenario, the fringe pattern is rotated to the scan direction, thus leads to poor dose contrast during exposure.

or pattern rotations occur, the resulting blurring or misalignment of the interference fringes leads to a reduced local intensity gradient. This causes a loss of dose contrast in the photo resist, making it more difficult to achieve sharp and uniform feature development.

The fringe period p is defined by the incident angles θ_1, θ_2 and the wavelength λ of the two exposure beams:

$$p = \frac{\lambda}{\sin(\theta_1) - \sin(\theta_2)}, \quad \theta_1 > 0, \ \ \theta_2 < 0. \tag{1}$$

The intensity distribution of the two interfering exposure beams in one dimension with equal polarization state is given as

$$\begin{aligned} I(x,t) &= (E_1 + E_2)(E_1 + E_2)^* \\ &= I_1 + I_2 + 2\sqrt{I_1 \cdot I_2} \cdot \cos[\Delta\varphi(x) + \varphi_{\mathrm{th}}(t)], \end{aligned} \tag{2}$$

where $\Delta\varphi(x)$ is the initial phase difference between the two exposure beams and $\varphi_{\mathrm{th}}(t)$ the time-dependent thermal phase fluctuation that causes the fringe shift. The Michelson contrast of the interference pattern is defined as

$$C_I = \frac{I_{\max} - I_{\min}}{I_{\max} + I_{\min}}. \tag{3}$$

While the position x of the fringes changes over the exposure time t_{exp}, the intensity in the photoresist is integrated, with the dose being defined by

$$D(x) = \int_0^{t_{\mathrm{exp}}} I(x,t)\,\mathrm{d}t. \tag{4}$$

The fringe shift by time results in a loss of dose contrast. The dose contrast is expressed as

$$C_D = \frac{D_{\max} - D_{\min}}{D_{\max} + D_{\min}}. \tag{5}$$

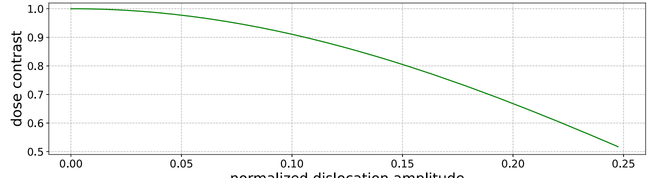

Figure 3. Dose contrast loss for a dislocation function $\varphi_{\mathrm{th}} = A \cdot \sin(\omega \cdot t)$. The maximum dislocation increases from zero to a quarter period of the intensity distribution.

This value quantifies the exposure process in the photoresist. A dose contrast loss simulation is shown in Figure 3. For illustration we define a sinusoidal function. Therefore the function is defined as follows:

$$\varphi_{\mathrm{th}} = A \cdot \sin(\omega \cdot t). \tag{6}$$

ω is the shift frequency and t the exposure time. The amplitude A defines the maximum fringe shift and for the dose contrast simulation in Figure 3, A increases from zero to a quarter period of the intensity distribution, so that the dose contrast is halved. With equations (6), (2), (4) and (5) the loss can be calculated for different dislocation amplitudes. The integration of $\omega \cdot t$ for the dose simulation is over one period.

3 Experimental setup

The writing head is designed to be installed in the nanopositioning and measuring machine NPMM-200, which is installed at the Institute of Applied Optics [21]. The stage in which the substrate can be placed is controlled by six interferometers. This provides high-precision distance and rotation measurement for six degrees of freedom and control for five degrees of freedom. The nano-scale positioning

extends over a very large volume of 200 mm × 200 mm × 25 mm. The entire stage is located in a large aluminum chamber to reduce influences such as air turbulence and temperature fluctuations. To quantify the performance of the writing head, a fringe observation system was implemented and placed instead of the substrate.

3.1 Writing head

Figure 4 shows the design of the writing head. There are basically two beam paths generated by two different laser sources, which are described in detail below. The laser source of the writing beam is a TOPTICA BlueMode laser head with a wavelength of 405 nm. The collimated beam with a diameter of 1.8 mm and a Gaussian intensity distribution (TEM_{00}) is divided by PBS2 into a horizontally polarized and a vertically polarized beam. Subsequently, the two beams are reflected by the mirrors M1 and M2 and interfere in the substrate plane. The half waveplate HWP2 rotates the linear polarization angle of the right beam, so the polarization states of both beams offer the best contrast of the interference pattern. The tilt of M1 and M2 defines the period p in the substrate plane.

The fringe locking laser is a HeNe laser from SIOS with a wavelength of 632.8 nm and a Gaussian intensity distribution (TEM_{00}). The fringe locking beam with a diameter of 2 mm is shifted laterally to the writing beam. After reflection at the mirrors the two fringe locking beams are reflected by a double prism retroreflector with an air gap between its short sides. At PBS2 both beams are recombined in the camera path and they interfere at the camera sensor. The achromatic half waveplate HWP1 at 45° ensures the equal splitting of both beams at PBS2. The quarter waveplates QWP 1 and 2 generate left and right circular polarization. After reflection at the retroreflector the circular polarization is reversed. By passing the QWPs again, the beams are completely transferred into the camera path with orthogonal polarization. The quarter waveplate QWP 3 in front of the polarization camera transfers the two beams into an orthogonal circular polarization state. This is important for the phase shifting method described in Section 3.2. Since the fringe locking beam has almost the same path geometry as the writing beam, the phase fluctuation approximates well the displacement of the writing spot on the substrate. As the reflection angle of the measuring beam in the retroreflector corresponds to the angle of incidence, the beams always hit the polarization camera at the same angle, regardless of the tilt of the mirrors M1 and M2. Only the lateral position of the interfering beams on the camera chip changes. This means that the tilts of M1 and M2 can be variably adjusted, allowing different fringe periods to be generated. M1 is mounted on a linear piezo actuator. The actuator is a P-753.1CD from Physics Instruments with an integrated capacitive position measuring sensor with a system resolution of 0.1 nm and positioning accuracy of 0.25 nm. The writing head was completely designed and simulated in the Optical CAD software Quaoda [22]. All mechanical and optical components are mounted on a breadboard with size of 180 × 230 mm^2 (see Fig. 5).

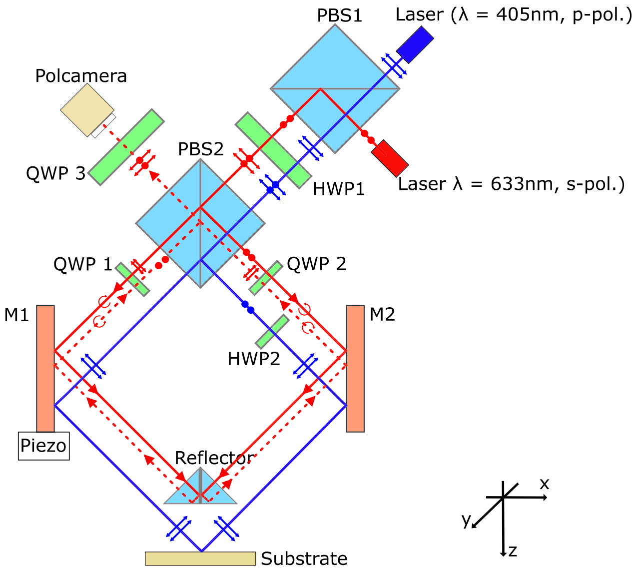

Figure 4. Optical scheme of the writing head. PBS: polarizing beam splitter, HWP: half waveplate, QWP: quarter waveplate, M: mirror.

3.2 Polarization interferometry

The FLIR Blackfly BFS-U3-51S5P-C polarization camera has a polarizer mask in front of the sensor. The mask contains four linear polarizers in the orientation 0°, 45°, 90° and 135°, arranged in a repeating pattern throughout the pixel range [23]. Four polarizer pixels define a superpixel, which contains all the information in a single camera frame to calculate the phase offset between the two beam paths (see Fig. 6). This spatial phase-shifting method is commonly used to measure the surface errors and topography of lenses and mirrors [24]. Each polarization channel generates a phase-shifted interferogram. This results in the following system of equations:

$$I_{0^\circ}(x, y) = A + B \cdot \cos\left[\Delta\varphi(x, y)\right], \tag{7}$$

$$I_{45^\circ}(x, y) = A + B \cdot \cos\left[\Delta\varphi(x, y) + \frac{\pi}{2}\right], \tag{8}$$

$$I_{90^\circ}(x, y) = A + B \cdot \cos\left[\Delta\varphi(x, y) + \pi\right] \tag{9}$$

$$I_{135^\circ}(x, y) = A + B \cdot \cos\left[\Delta\varphi(x, y) + \frac{3}{2}\pi\right] \tag{10}$$

where $A = I_1 + I_2$ and $B = 2\sqrt{I_1 \cdot I_2}$. With this system of equations the phase difference $\Delta\varphi(x, y)$ for each superpixel x, y can be determined:

$$\Delta\varphi(x, y) = \arctan\left[\frac{I_{90^\circ}(x, y) - I_{0^\circ}(x, y)}{I_{135^\circ}(x, y) - I_{45^\circ}(x, y)}\right]. \tag{11}$$

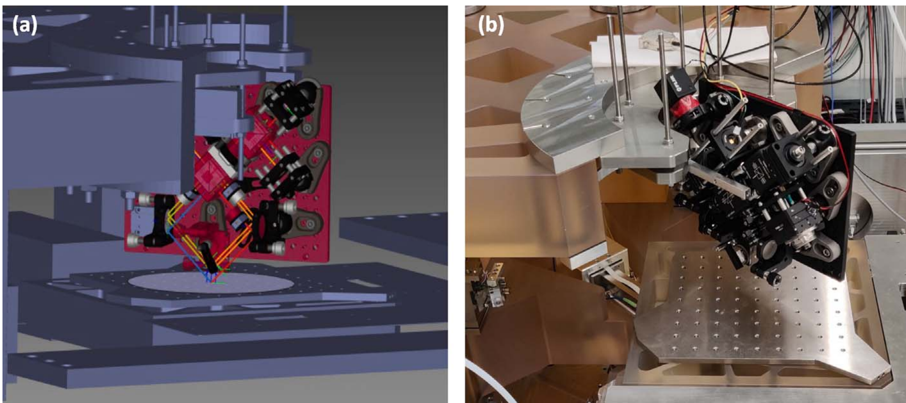

Figure 5. (a) Quadoa model of the SBIL writing head. (b) Photo of the SBIL writing head integrated into the NPMM-200.

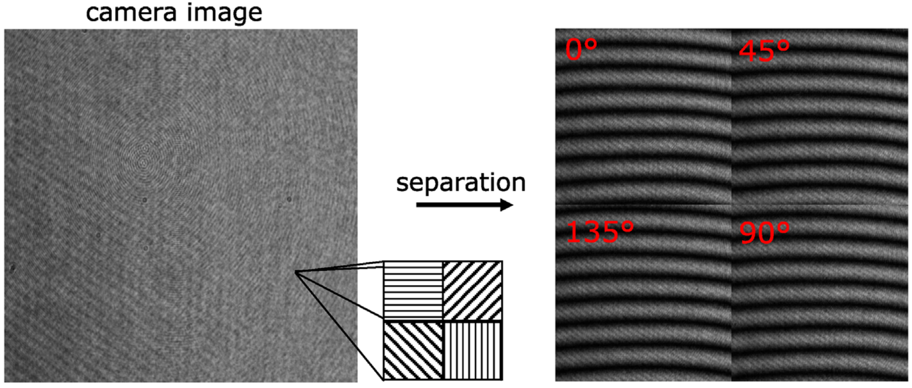

Figure 6. Scheme of polarization camera based interferometry. After an image has been captured, the individual polarization channels are sorted and the phases of the superpixels are calculated according to equation (11). An example measurement is shown on the right. The interference fringes, which are phase-shifted to each other, are clearly visible.

After unwrapping the modulo 2π phase map $\Delta\varphi(x, y)$, the Zernike coefficients are calculated by use of a least-square fit with Zernike polynomials. Accordingly, the phase difference and the tilt in the x- and y- directions can be determined quantitatively. The area-based measuring method can also be used to correctly align the mirrors to each other before the exposure process. The position of the interferogram on the camera sensor provides information about the tilt angle of the two mirrors and therefore about the period of the exposure pattern on the substrate. Furthermore, the overlap of the two beams in the camera image ensures that both mirrors reflect the writing beams onto the substrate at the correct angles. Another important feature is the detection of the fringe orientation, which is defined by the rotation of the mirrors around the z-axis. This characteristic will be investigated in Section 4.

3.3 Closed loop control

Before exposing the photoresist, an initial state "init" of the fringe locking signal with the desired design parameters of the fringe pattern is defined, i.e. in terms of fringe period, fringe orientation and fringe offset. The measured wavefront W_{init} on the polarization camera can be approximated by a fit with Zernike polynomials with a given circular aperture:

$$\begin{aligned} W_{\text{init}}(r,\theta) &= \sum_{n=0}^{1}\sum_{m=-1}^{n}(c_n^m)_{\text{init}}\cdot Z_n^m(r,\theta) \\ &= \underbrace{(c_0^0)_{\text{init}}\cdot Z_0^0}_{\text{Piston}} + \underbrace{(c_1^{-1})_{\text{init}}\cdot Z_1^{-1}}_{\text{Tilt } y} + \underbrace{(c_1^{+1})_{\text{init}}\cdot Z_1^{+1}}_{\text{Tilt } x}. \end{aligned} \tag{12}$$

The current state at a specific time t can be written as

$$W_t(r,\theta) = (c_0^0)_t\cdot Z_0^0 + (c_1^{-1})_t\cdot Z_1^{-1} + (c_1^{+1})_t\cdot Z_1^{+1}. \tag{13}$$

Finally, the deviation d from the initial state at time t can be expressed as

$$W_d(r,\theta,t) = W_{\text{init}}(r,\theta) - W_t(r,\theta). \tag{14}$$

whereby the individual deviations can be specified as follow:

Fringe Offset:

$$(c_{\text{offset}})_d = (c_0^0)_{\text{init}} - (c_0^0)_t. \tag{15}$$

Period drift:

$$(c_{\text{tilt}})_d = \sqrt{(c_1^{-1})^2_{\text{init}} + (c_1^{+1})^2_{\text{init}}} - \sqrt{(c_1^{-1})^2_t + (c_1^{+1})^2_t}. \tag{16}$$

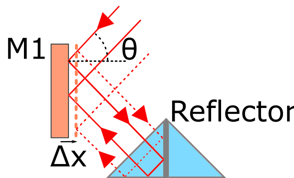

Figure 7. Displacement of M1 by Δx leads to a different optical path. The dashed lines indicate the displacement of the mirror and the resulting path change.

Fringe pattern rotation:

$$(c_{\text{rotation}})_d = \arctan\left[\frac{(c_1^{-1})_{\text{init}}}{(c_1^{+1})_{\text{init}}}\right] - \arctan\left[\frac{(c_1^{-1})_t}{(c_1^{+1})_t}\right]. \quad (17)$$

Due to the reflection at the double prism reflector, a lateral displacement with a piezo actuator of M1 by Δx_{M1} affects a phase shift of the fringe locking beam $\Delta\varphi$ as follows:

$$\Delta\varphi = \frac{2\pi}{\lambda}[4\cos(\theta)\,\Delta x_{\text{M1}}], \quad (18)$$

where θ is the incident angle of the exposure beam and the pre-factor 4 results from the double reflection at the mirror and thus the double passage through the beam path, see Figure 7. The detailed operating principle of the closed-loop system has been reported in [25].

3.4 Fringe observation system

In order to determine the shift of the interference fringes for calibration and to evaluate the performance of the fringe locking system, a fringe observation system was implemented. A Olympus microscope objective lens (UMPlanFI) with a numerical aperture of 0.95 was placed at the position of the substrate (see Fig. 8a). After the microscope objective, the beams are reflected by a tilted mirror. To image the fringes on the camera chip, a tube lens (TL) with a focal length of $f' = 100$ mm was used. The camera used is a Ximea MC124MG-SY-UB with a pixel pitch $x_{\text{pixel}} = 3.45$ µm. The integration time was set to 50 ms, corresponding to an effective sampling rate of approximately 20 Hz. Consequently, higher-frequency stage vibrations are temporally averaged by the camera integration and are therefore not directly resolved in the measurements. The result can be seen in Figure 8b. In a next step, the fringe motion is monitored over time. To quantify the fringe displacement in nanometers, the Fourier-transform method [19] was used. The single steps of the algorithm are visualized in Figure 9. At first, the initial image with 160 × 160 pixels is 2D-Fourier transformed. The area around the main frequency peak (rectangle marked in red) with 30 × 30 pixels is shifted to the 2D-Fourier center, i.e. to remove the carrier frequency of the interference pattern. Since only low-frequency changes are examined, all other frequencies are set to zero to minimize noise. With the inverse Fourier-transform, the phase can be calculated from the real part and the imaginary part. Afterwards, the wavefront is unwrapped and a fit with Zernike polynomials within the circular aperture marked in red is applied. For reference measurements, an initial state is also defined as described in Section 3.3.

The unambiguity range of the fringe movement is half of the fringe period p. One fringe period extends over approximately $N_{\text{pixel}} = 3$ pixels in diagonal in the camera image. With a period of $p = 270$ nm, the lateral magnification factor M_L can calculated by

$$M_L = \frac{N_{\text{pixel}} \cdot \sqrt{2}\, x_{\text{pixel}}}{p} = \frac{3 \cdot 3.45 \cdot 10^{-6}\text{m} \cdot \sqrt{2}}{270 \cdot 10^{-9}\text{m}} = 54.21, \quad (19)$$

where the factor $\sqrt{2}$ is given by the diagonal of the pixels. The fringe displacement resolution of this setup was estimated using simple simulations. For this purpose, a stack of fringe images with well-defined displacement was generated. The magnification factor, the pixel pitch and the image size of the observation system were taken into account. The Fourier method was then applied. This leads to a resolution in the sub-nanometer range. The observation system is mounted on the NPMM-200 stage made from Zerodur and Invar. It's position is interferometrically controlled.

4 Experimental results

In SBIL systems, the fringe pattern must be stabilized not only in its lateral position, but also in its rotation, i.e. it must be stationary. In this section we first present the tracking of the fringe rotation. We then present the performance of the fringe locking system. All results are compared and evaluated with the fringe observation system described in Section 3.4. The lasers in the writing head were switched on before measurements so that the built-in optics could warm up and thermal expansion during the measurements could be avoided. The data sets are evaluated with the python developer environment ITOM [26]. The average time delay from the recorded camera image to the piezo controller is 17 ms. With a sampling rate of 60 Hz, the fringe locking system is able to detect and compensate for the drifts of the writing head.

4.1 Fringe rotation tracking

Rotating mirror M2 by angle β around the z-axis, the fringe orientation of the writing spot will change by angle γ, as shown in Figure 10. The overlap area of the two exposure beams also changes slightly, but is neglected due to small changes. Due to the Gaussian intensity profile of the writing spot, these non-interfering regions are located at the outer edges of the beam where the intensity is significantly reduced. Consequently, their contribution to the effective exposure dose of the photoresist is minimal and does not lead to a noticeable spreading.

In order to characterize the angular sensitivity of the fringe locking system, M2 is tilted in different steps in a specified time. During this time, the interferograms of the fringe locking signal and the fringe observation system are captured. The Zernike polynomials Z_1^{+1} and Z_1^{-1} are fitted

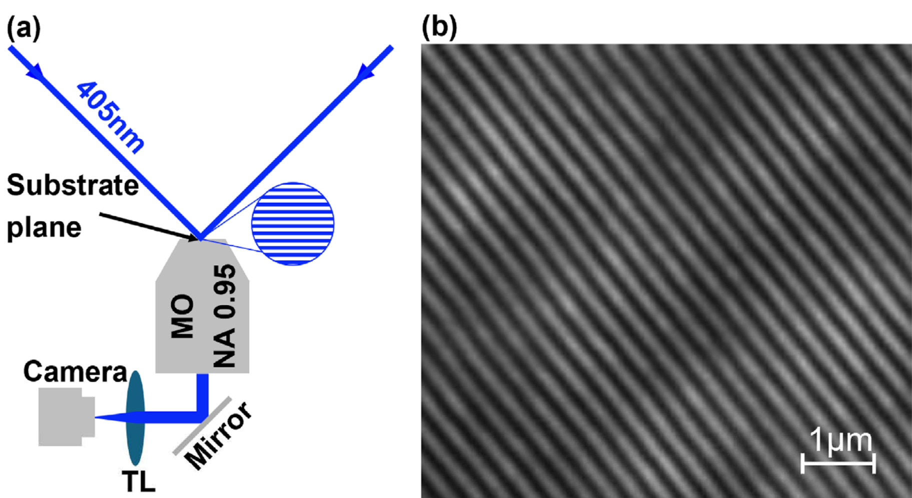

Figure 8. (a) Draw of the fringe observation system. (b) Captured image of the writing spot fringes.

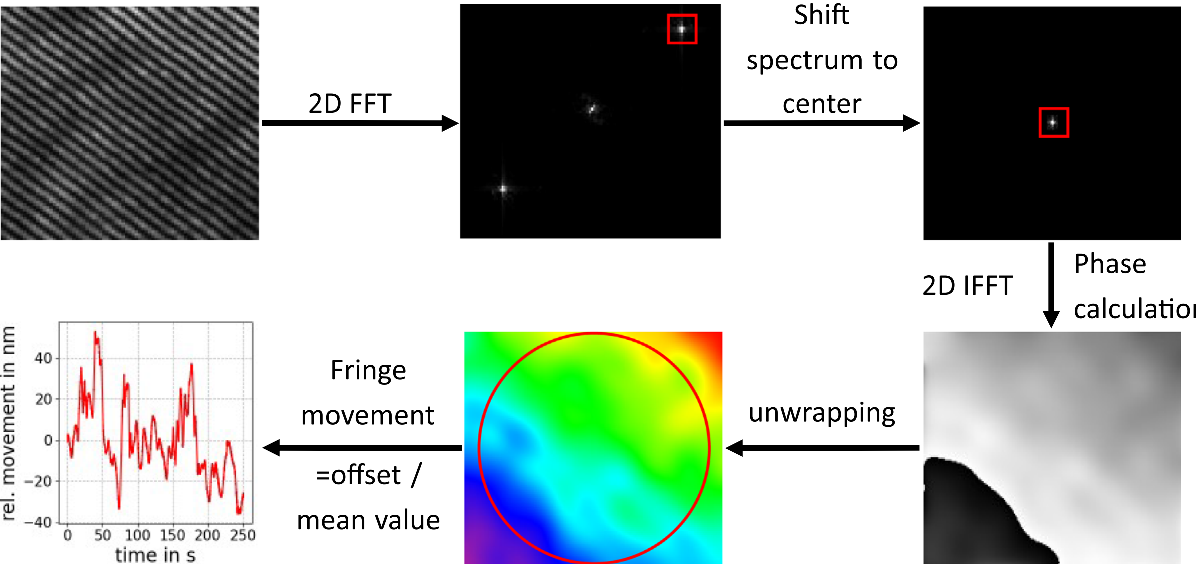

Figure 9. Scheme of the Fourier-transform method [19] to determine the fringe movement of the captured image in the fringe observation system.

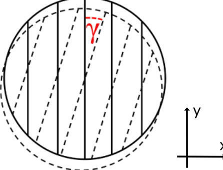

Figure 10. Fringe rotation γ within the writing spot in the substrate plane, due to mirror rotation. The solid circle shows the writing spot with perfect overlapping of the exposure beams. If one of the mirrors M1 or M2 rotates around the z-axis, the exposure beam moves on a circular track. For this reason the spots are not overlapping completely and the fringes change their direction.

to obtain the Zernike coefficients c_1^{+1} and c_1^{-1}, as explained in Section 3.3. The angle γ is given by equation (17). Spherical coordinates are used to describe the propagation direction with the wave vector $\mathbf{k}$.

$$\mathbf{k}(\theta, \beta) = \begin{pmatrix} k_x \\ k_y \\ k_z \end{pmatrix} = |\mathbf{k}| \cdot \begin{pmatrix} \sin(\theta)\,\cos(\beta) \\ \sin(\theta)\,\sin(\beta) \\ \cos(\theta) \end{pmatrix}. \qquad (20)$$

The results are shown in Figure 11. Within 60 seconds, five movements of M2 were performed manually. Both measurement systems captured the fringe rotation. The measurement sensitivity depends on the ratio between the incident angles of the two beams θ and the mirror rotation β.

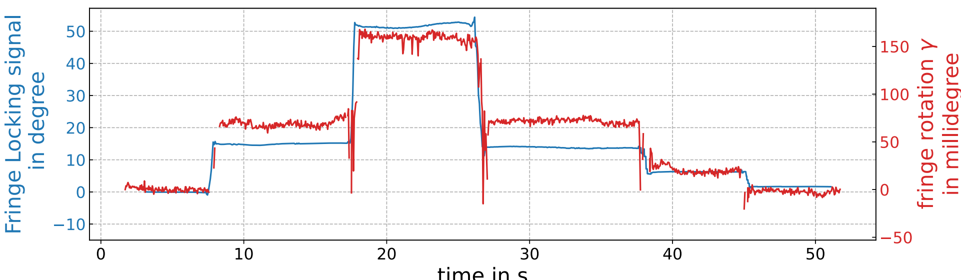

Figure 11. Rotation measurement. The rotation was calculated with equation (17) after performing a least square fit of the Zernike polynomials Z_1^{+1} and Z_1^{-1}.

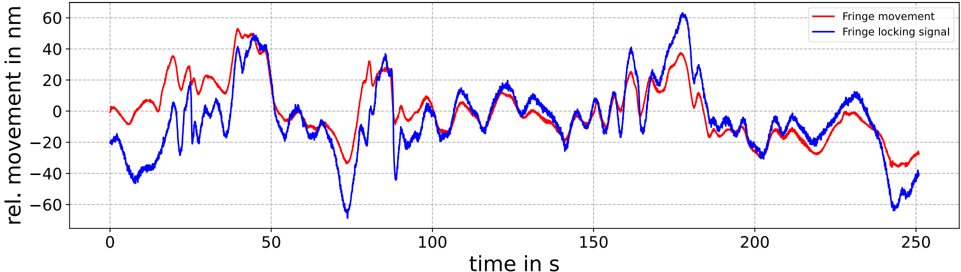

Figure 12. Phase fluctuation measurement without fringe locking. The piezo is not moving during the measurement.

In terms of equation (20), θ and β are approximately equal in the fringe locking camera path, leading to nearly equal vector components k_x and k_y. That means that small tilts in β greatly rotate the interfering wavefront in the camera path. The signal of the fringe observation system is not that sensitive, because θ is with around 45° much larger than β. The fringes rotate around 0.17° in contrast to the fringe locking signal with 55° of the rotation range.

In addition, it can be observed that the signals between the measurement systems are not linear to each other. This is caused by the retroreflector. The propagation direction of the reflected beams in the retroreflector strongly depends on the orientation of the prism surfaces. The two prisms are not perfectly aligned with each other. A slight misalignment directly causes a low-frequency fringe image on the camera, as the two beams are no longer parallel to each other in the camera arm. To take into account the misalignment of the two prisms, we introduce prefactors a that depend on the angles θ and β.

$$\mathbf{k}(\theta,\beta) = |\mathbf{k}| \cdot \begin{pmatrix} a_x(\theta,\beta)\cdot\sin(\theta)\cos(\beta) \\ a_y(\theta,\beta)\cdot\sin(\theta)\sin(\beta) \\ a_z(\theta,\beta)\cdot\cos(\theta) \end{pmatrix}. \tag{21}$$

With this equation, the nonlinearity can be compensated by calibration measurements. The calibration must be repeated for each alignment in terms of θ.

4.2 Fringe locking

At first the phase fluctuation of the test environment was identified. In Figure 12, the measurement shows a low-frequency fringe displacement with 85 nm peak-to-valley (red line) and with an RMS value of 18.33 nm in a time range of 250 s.

The phase fluctuation is mainly caused by air turbulence in the beam paths. The dose contrast, according to equation (5), for this measurement is 0.793, compared to the mean contrast of a single intensity distribution of equation (3) with 0.867. This results in a contrast loss of 7.4%. Although the phase fluctuations determined with the fringe locking system and the fringe observation system differ slightly, the characteristic features are still clearly recognizable. The camera of the observation system is placed below the writing head.

During measurements, the camera induces heat turbulence, which increases the temperature of the retroreflector. This induces different air fluctuations in the fringe locking beam path, which finally leads to partial differences between the measurement data. However, with a correlation coefficient [27] of $R = 0.749$, the two measurements strongly correlate. In a next step, the piezo actuation was calibrated. A sinusoidal oscillation with an amplitude of 1 μm was induced. Due to the dominant amplitude, air turbulence can be neglected during calibration. The fringe movement in the substrate plane is again captured by the fringe observation system (see Fig. 13). As the movement of the fringes here is greater than the unambiguous range $\frac{p}{2}$ of the evaluation of the fringe observation system, the measurement data were unwrapped over the time axis. Then a sine function was fitted to the red curve to determine its amplitude. The ratio of the two amplitudes results in the transfer factor of the piezo movement to the fringe movement in the substrate plane. The factor was determined to be 0.63. Finally, the fringe locking was tested in closed loop. In Figure 14 the fringe locking signal (blue line),

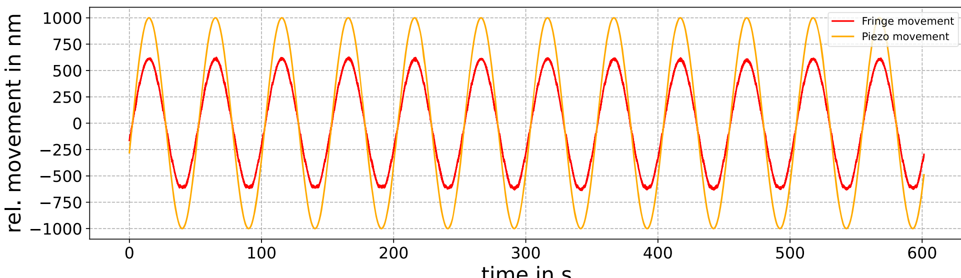

Figure 13. Piezo calibration measurement. The different amplitude of the sinusoidal curves gives the transfer factor between the piezo movement of mirror M1 and the fringe movement in the substrate plane.

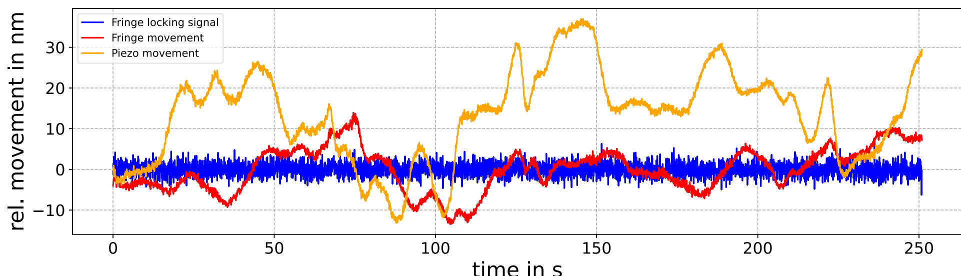

Figure 14. Phase fluctuation measurement with enabled fringe locking. The fringe locking signal is controlled to zero by moving the piezo. The fringe observation system shows a greatly reduced movement of the fringes in the substrate plane.

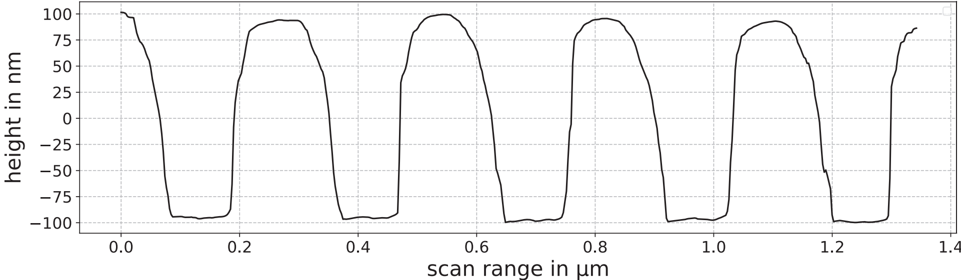

Figure 15. AFM measurement of a linear grating in photoresist. The grating depth is approx. 192 nm ± 3 nm.

the piezo movement (orange line) and the fringe movement in the substrate plane (red line) are visualized. The fringe locking signal is controlled to zero by moving the piezo. The RMS value of the fringe locking signal in closed-loop is 1.48 nm. The fringe movement is significantly reduced. Between 75 s and 110 s the fringe locking was more influenced by the heat turbulence of the observation camera, so that the peak-to-valley movement is around 25 nm with an RMS value of 5.29 nm. For the lithography process with photo resist, the heat of the observation camera would not disturb the fringe locking. During closed loop control, the movement of the fringes with a period $p = 270$ nm was mainly reduced to ±5 nm. This translates to a PV-wavefront reconstruction quality of approx. $\frac{\lambda}{25}$ at such small periods. The mean intensity contrast of the fringes is 0.839. The dose contrast is 0.827. With fringe locking control enabled, the contrast loss was reduced from 7.4% to 1.2%. For first lithography tests, the fringe observation system was replaced by a substrate with positive photoresist

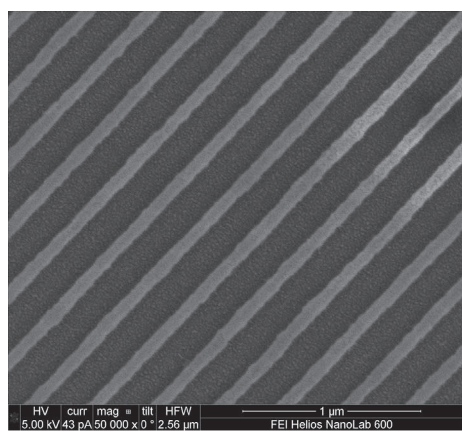

Figure 16. SEM image of the linear grating in photoresist, sputtered with gold to avoid charging effects. The determined period of the structures is $p = 270$ nm (±2 nm).

(AZ MIR 701 from MicroChemicals) with thickness $d =$ 195 nm. With a scanning electron microscope and an atom force microscope, the grating period was determined to $p = 270$ nm (± 2 nm) (see Figs. 15 and 16).The grating depth was determined to around $h = 192$ nm.

5 Conclusion

A new fringe stabilization system for an SBIL system was presented. Using polarization camera-based real-time interferometry, the phase shift and the orientation of the two exposure beams are recorded with a separate measuring beam. This allows the lateral fringe movement and the orientation of the fringe pattern in the substrate plane to be precisely determined. A fringe observation system was implemented, which was placed in the substrate plane. Due to the high positioning accuracy of the nano positioning and measuring machine NPMM-200, the movement of the fringe pattern is precisely measured. Without fringe locking, the fringes moved a few tens of nanometers due to air turbulence and the dose contrast loss was 7.4%. Our results demonstrate that activation of the fringe locking system effectively reduced fringe displacement to ± 5 nm. This improves the wavefront error in the reconstruction to less than $\frac{\lambda}{25}$ and reduces the contrast loss to 1.2%. It should be noted that these values were detemined for $p = 270$ nm and scale with the grating period. For larger periods, the expected improvements are even better. Furthermore, the fringe locking system was also used to determine the fringe rotation in situ in the substrate plane. A rotation test demonstrated highly precise sensitivity in the millidegree range. Finally, structures were fabricated in photoresist with a period of approx. 270 nm and a grating depth of 192 nm. Improvements to this system are planned for future work. The measurements with the fringe observation system have shown that the camera heat influences the phase fluctuations and thus the fringe stabilization. A cooling system is therefore planned to minimize the disturbance and achieve fringe stability in the subnanometer range. In addition, the mirrors can be equipped with piezo actuators to compensate for fringe rotation or to compensate for rotary stage errors.

Funding

The FIB-SEM FEI Helios NanoLab 600 was funded by the Deutsche Forschungsgemeinschaft (DFG, German Research Foundation) – 154585072. The nano positioning and measuring machine NPMM-200 was funded by the Deutsche Forschungsgemeinschaft (DFG, German Research Foundation) – 267094782 Funding This work was supported by German Research Foundation (Deutsche Forschungsgemeinschaft, DFG), grant no. 465642714.

Conflicts of interest

The authors declare that they have no competing interests to report.

Data availability statement

Data underlying the results presented in this paper are not publicly available at this time but may be obtained from the authors upon reasonable request.

Author contribution statement

Conceptualization K.T., J.R., H.W., I.O., C.P., C.S. T.H., O.S., E. M., T.K. and S.R.; Methodology C.P., C.S., T.H., O.S., E.M., T.K. and S.R.; Software, K.T., H.W., C.S. and J.R.; Investigation K.T., J.R., H.W. and C.P.; Writing – Original Draft Preparation K.T.; Writing – Review Editing K.T., J.R.,C.P. I.O., T.H., O.S., E.M., T.K. and and S.R.; Project administration T.H., O.S., E.M., T.K. and S.R.; Funding acquisition T.H., O.S., E.M.

References

1 Kneubühl F, Diffraction grating spectroscopy, Appl. Opt. 8 (3), 505–519 (1969). https://doi.org/10.1364/AO.8.000505.
2 Ronchi V, Forty years of history of a grating interferometer, Appl. Opt. 3, 437–451 (1964). https://doi.org/10.1364/AO.3.000437.
3 Martz DH, Nguyen HT, Patel D et al., Large area high efficiency broad bandwidth 800 nm dielectric gratings for high energy laser pulse compression, Opt. Express 17(26), 23809–23816 (2009). https://doi.org/10.1364/OE.17.023809.
4 Ahmed MA, Beirow F, Loescher A et al., High-power thin-disk lasers emitting beams with axially-symmetric polarizations, Nanophotonics 11, 835–846 (2022). https://doi.org/10.1515/nanoph-2021-0606.
5 Peeters R, Lok S, Mallman J, et al., EUV lithography: NXE platform performance overview, Proc. SPIE 9048, Extreme Ultraviolet (EUV) Lithography V (2014). https://doi.org/10.1117/12.2046909.
6 Guoguang Y, Yibing S, Research on laser direct writing system and its lithography properties, SPIE Vol. 3550 (1998).
7 Poleshchuk AG, Churin EG, Koronkevich VP, et al., Polar coordinate laser pattern generator for fabrication of diffractive optical elements with arbitrary structure, Appl. Opt. 38(8), 1295–1301 (1999). https://doi.org/10.1364/AO.38.001295.
8 Schattenburg M, Chen C, Everett P, Ferrera J, Konkola P, Smith H, Sub-100 nm metrology using interferometrically produced fiducials, J. Vac. Sci. Technol. B 17, 2692–2697 (1999). https://doi.org/10.1116/1.591047.
9 Bienert F, Graf T, Ahmed MA, Comprehensive theoretical analysis of the period chirp in laser interference lithography, Appl. Opt. 61(9), 2313–2326 (2022). https://doi.org/10.1364/AO.451873.
10 Chen CG, Konkola PT, Heilmann RK, Joo C, Schattenburg ML, Nanometer-accurate Grating Fabrication with Scanning Beam Interference Lithography, Proc. SPIE 4936 (2002). https://doi.org/10.1117/12.469431.
11 Chen C, Konkola P, Heilmann R, Pati G, Schattenburg M, Image metrology and system controls for scanning beam interference lithography, J. Vac. Sci. Technol. B 19, 2335–2341 (2001). https://doi.org/10.1116/1.1409379.
12 Young P, Priambodo P, Maldonado T, Magnusson R, Simple interferometric fringe stabilization by CCD-based feedback control (Optical Society of America, 2005). https://doi.org/10.1364/FIO.2003.WJ6.

13 Häfner M, Pruss C, Osten W, et al., Fabrication of rotational symmetric sub wavelength grating structures, DGaO Proceedings (2008).
14 Lu S, Yang K, Zhu Y, Wang L, Zhanga M, Analysis and design of fringe phase control system for scanning beam interference lithography, Opt. Eng. 60(6), 064107 (2021). https://doi.org/10.1117/1.OE.60.6.064107.
15 Chen CG, Heilmann RK, Joo C, Konkola PT, Pati GS, Schattenburg ML, Beam alignment for scanning beam interference lithography, J. Vac. Sci. Technol. B 20, 3071–3074 (2002). https://doi.org/10.1117/1.OE.60.6.064107.
16 Chen X, Jiang S, Li Y, Jiang Y, Wang W, Bayanheshig, Fabrication of ultra-high aspect ratio silicon grating using an alignment method based on a scanning beam interference lithography system, Opt. Express 30, 40842–40853 (2022). https://doi.org/10.1364/OE.469374.
17 Li M, Xiang X, Zhou C, Wei C, Scan angle error measurement based on phase-stepping algorithms in scanning beam interference lithography, Appl. Opt. 58, 2641–2649 (2019). https://doi.org/10.1364/AO.58.002641.
18 Li Y, Jiang S, Chen X, Liu Z, Wang W, Song Y, Bayanheshig, Accurate measurement and adjustment method for interference fringe direction in a scanning beam interference lithography system, Opt. Express 31, 28145–28160 (2023). https://doi.org/10.1364/OE.485488.
19 Takeda M, Ina H, Kobayashi S, Fourier-transform method of fringe-pattern analysis for computer-based topography and interferometry, J. Opt. Soc. Am. 72, 156–160 (1982). https://doi.org/10.1364/JOSA.72.000156.
20 Jäger G, Manske E, Hausotte T, Müller A, Balzer F, Nanopositioning and nanomeasuring machine NPMM-200 – a new powerful tool for large-range micro- and nanotechnology, Surf. Topogr.: Metrol. Prop. 4(3), 034004 (2016). https://doi.org/10.1088/2051-672X/4/3/034004.
21 Schober C, Pruss C, Herkommer A, Osten W, The NPMM-200: large area high resolution for freeform surface measurement (Proc. SPIE, 2020). https://doi.org/10.1117/12.2564918.
22 Quadoa Optical CAD (2024). https://www.quadoa.com/index.
23 Sony Semicon (2024), IMX250/264/253MZR/MYR Sensor Flyer. https://www.sony-semicon.com/files/62/flyer_industry/IMX250_264_253MZR_MYR_Flyer_en.pdf.
24 Millerd JE, Brock NJ, Hayes JB, North-Morris MB, Novak M, Wyant JC, Pixelated Phase-Mask Dynamic Interferometer, Proc. SPIE 5531 (2004). https://doi.org/10.1117/12.560807.
25 Rühle J, Treptow K, Schober C, et al., Polarization camera based fringe locking control of a writing head for scanning beam interference lithography, Proc. American Control Conference (ACC) (2025). https://doi.org/10.23919/ACC63710.2025.11107550.
26 ITOM (2024). https://itom-project.github.io/documentation.html.
27 Sedgwick P., Pearson's correlation coefficient, BMJ 345, e4483 (2012). https://doi.org/10.1136/bmj.e4483.